Flow-induced channel formation in the cytoplasm of motile cells

Robert D. Guy[*]
Department of Mathematics, University of California Davis, Davis, California, USA

Toshiyuki Nakagaki[†]
Department of Complex and Intelligent Systems, Faculty of Systems Information Science, Future University Hakodate, Hakodate, Japan

Grady B. Wright[‡]
Department of Mathematics, Boise State University, Boise, Idaho, USA

(Received 9 November 2010; revised manuscript received 11 May 2011; published 18 July 2011)

A model is presented to explain the development of flow channels within the cytoplasm of the plasmodium of the giant amoeba *Physarum polycephalum*. The formation of channels is related to the development of a self-organizing tubular network in large cells. Experiments indicate that the flow of cytoplasm is involved in the development and organization of these networks, and the mathematical model proposed here is motivated by recent experiments involving the observation of development of flow channel in small cells. A model of pressure-driven flow through a polymer network is presented in which the rate of flow increases the rate of depolymerization. Numerical solutions and asymptotic analysis of the model in one spatial dimension show that under very general assumptions this model predicts the formation of channels in response to flow.

DOI: 10.1103/PhysRevE.84.016310 PACS number(s): 47.63.−b, 05.45.−a, 47.50.−d, 47.54.−r

I. INTRODUCTION

The true slime mold *Physarum polycephalum* is a single-cell amoeboid organism reaching up to meters in size (see Fig. 1). They can be found on the forest floor among decaying leaves and rotten wood where it is dark, damp, and cool. The plasmodium is the vegetative stage in its life cycle, and it has been a standard model organism for studying cellular rhythms and active cytoplasimc streaming for over 70 years [1].

The cell generates flows of cytoplasm with velocities up to 1 mm/s in order to transport nutrients and communicate chemical signals over the large distances spanned by the cell body. The cytoplasm is made of two phases of material: endoplasm (cytosol) and ectoplasm (cytoskeleton). The endoplasm includes water with dissolved ions, small proteins, and vesicles. The ectoplasm consists of a filamentous network of actin which forms the outer cortical gel. The fluid flow of cytosol is driven by organized rhythmic contractions of the gel with a period of about 2 min. The tension within the gel is generated by actin-myosin contraction and results in internal pressure gradients. The back and forth motion of the sol that results is called shuttle streaming [1,2]. The rhythmic contraction is observed everywhere within the cell and is driven by biochemical oscillations involving Ca^{2+}, ATP, H^+, cAMP, NAD(P)H^+, phospholipid, etc. [3–9].

The cell is organized as a network of highly adaptable tubular elements, which repeatedly bifurcate from thick tubes to smaller tubes (see Fig. 1). The cytoplasm flows through this tubular network, which serves as a circulation system for the cell. The walls of these tubes are made of a thick ectoplasmic gel. It is not known how the cytoplasm organizes into these tubular networks, but there is substantial experimental evidence that the flow of cytoplasm is involved in both the initiation and regulation of the network [10,11].

The adaptability of the tubular network endows the cell with the ability to process spatial information. For example, it can accomplish tasks such as identifying the shortest path in a maze [12,13]. A number of other more general computational abilities related to the dynamics of the network have been reported [14–16]. Mathematical models have been developed which demonstrate how adaptable structures can be used to process information [17,18], but these models were phenomenological; they do not address the mechanism of how the tubes reorganize. In this paper, we study the early development of tubular structures. In the frontal region of the plasmodium, the cell is not organized into tubular structures. This region is like a porous medium in which the cytosol is driven through the cytoskeleton by pressures generated from contractions of the cortical gel. Within this region, flow channels develop in which the concentration of cytoskeleton is low and the velocity of cytosol is much larger than in nearby regions with higher gel concentrations. These flow channels eventually develop into tubular structures, and so a first step to understanding tubular development is exploring the mechanisms involved in flow channel formation.

When the organism is small (less than 100 μm) there is no shuttle streaming and no structural organization of the cell body. As it gets larger, flow channels develop within the gel, streaming begins, and the cell begins to migrate faster [19,20]. Recent experiments on these small cells show that channels form suddenly in response to intracellular flow, thus indicating a flow-induced instability within the sol/gel mixture [20]. In this paper we propose and analyze a mathematical model of the pressure-driven flow of cytoplasm including the interaction between the sol and gel. The cytosol experiences frictional resistance as it is driven through the networked actin gel. We show that when the frictional force from the fluid increases the depolymerization rate of the polymer, flow channels result. The

[*]guy@math.ucdavis.edu
[†]nakagaki@fun.ac.jp
[‡]gradywright@boisestate.edu

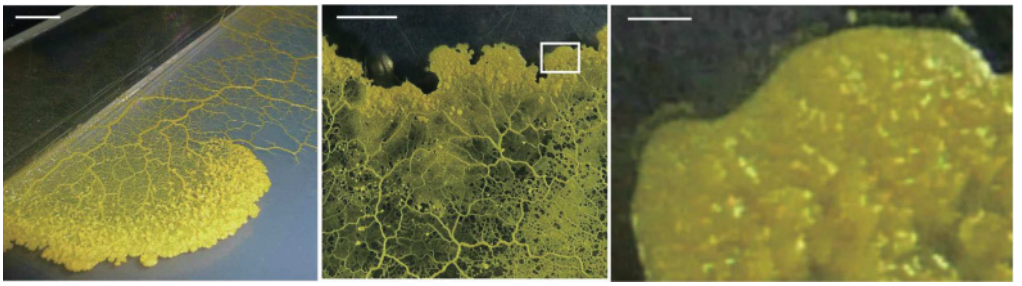

FIG. 1. (Color online) Macroscopic images of *Physarum* plasmodium. The frontal region of the plasmodium takes the form of sheet-like structure, and a complicated network of veins develops toward the rear. Flow channels develop within the cytoskeleton of the frontal region as the cytosol bores though this dynamic porous medium. These channels eventually develop into mature veins. In this paper, we study the mechanism of channel initiation. Scale bars are 1 cm (right and center panels) and 1 mm (left panel).

model predicts hysteretic behavior of the flow of cytoplasm in response to the applied pressure. There is a critical pressure at which channels appear, and a lower critical pressure at which channels disappear. Using asymptotic analysis in the phase plane, we show that the qualitative model behavior is very generic. That is, the behavior exhibited by the numerical solution is not sensitive to our assumptions.

The remainder of the paper is organized as follows. In Sec. II we describe recent experiments on intracellular flow and channeling which motivate the development of the model. In Sec. III we present the mathematical model and the results of numerical explorations. In Sec. IV we present asymptotic analysis to explain the behavior of the model observed numerically, and we give general conditions that lead to channeling. Finally, in Sec. V we argue that the qualitative behavior of the model is generic, and we comment on the significance of the results.

II. EXPERIMENTAL OBSERVATION OF CHANNEL FORMATION

We performed experiments on small plasmodia to observe the initiation of flow channels, shuttle streaming, and locomotion. We processed video images of the cells to tract the motion of intrinsic vesicles. Using particle image velocity (PIV), we calculated the velocity of cytoplasmic streaming inside the cell and the deformation of the cell shape. The details of the experiments are given in [20].

In Fig. 2(a) we show typical unprocessed image of the cell before streaming begins, and in Fig. 2(b) we show the processed image which is created by the superposition of the positive part of the enhanced image over several seconds. The moving vesicles appear as elongated dark spots. Before streaming there is no organized flow pattern within the cell. In Fig. 2(c) we show the processed image after streaming has been initiated. The dark region running through the middle of the cell indicates the presence of a flow channel.

After streaming begins, the cell body becomes elongated in the direction of the flow channel, and it begins to migrate. It takes on a tadpole-like shape with a flow channel running along the tail, connected to a head which is initially devoid of channeled structures. This is illustrated in Fig. 3(d), in which the intracellular velocity field and boundary velocity have been overlaid on the image. The sol flows much more slowly through the porous, gel-filled head region than through the channel in the tail, as can be seen in Fig. 3(b), where the lighter pixels correspond to faster flows. In Figs. 3(c) and 3(e) the same cell is shown one period later (100 s). A new flow channel has appeared in the head region. This sudden rather than gradual development of the new channel indicates that channel formation involves a critical phenomenon or a bifurcation.

In Fig. 3(a) we show the magnitude of the velocity field along the dashed lines in Figs. 3(b) and 3(c) which is perpendicular to the direction of flow. The velocity is shown at five equally spaced time points 50 s apart (every 1/2 period). At time points 1–3 the speed of the flow is relatively uniform across the cell, but at time points 4 and 5 the velocity is about four times larger in the middle portion of the cell compared to the edges. Between the measurements at times 3 and 4, a flow channel appeared.

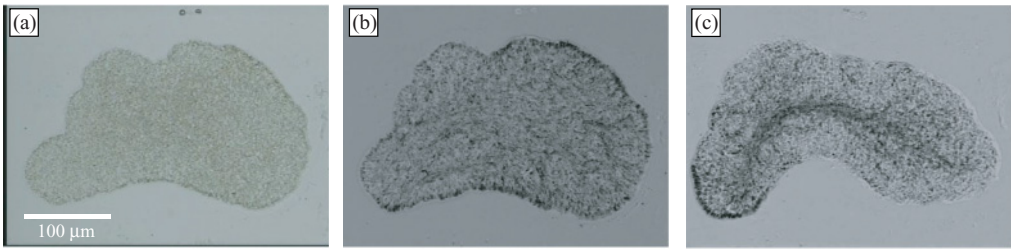

FIG. 2. (Color online) (a) Unprocessed image of a small plasmodium before the onset of shuttle streaming. (b) Processed image to show the magnitude of the velocity. Dark pixels correspond to faster flow. (c) The onset of streaming is accompanied by the formation of a flow channel, which corresponds to the dark region in the middle of the cell. Scale bar is 100 μm.

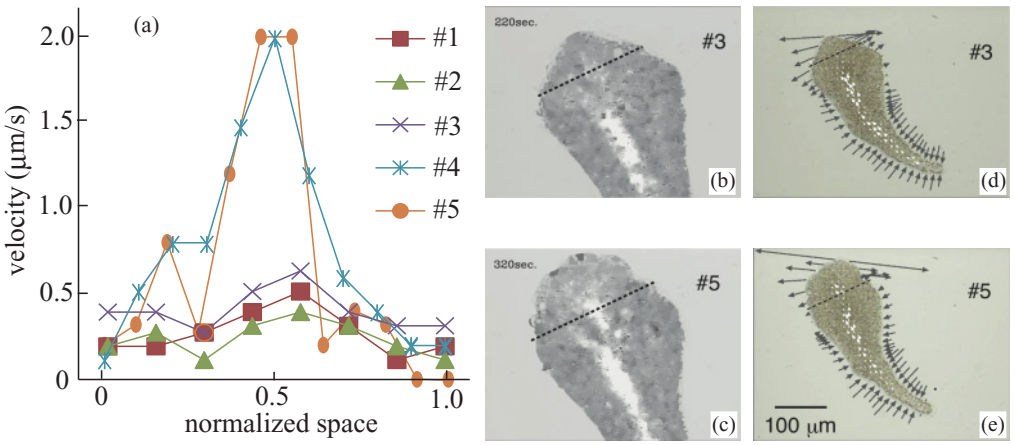

FIG. 3. (Color online) (a) Magnitude of velocity along a line normal to the direction of migration in the frontal part of the migrating cell shown at five 50 s time intervals (every half period of the oscillation). At time points 1–3 the velocity is relatively uniform across the cell, and at times 4 and 5 the velocity is about four times larger in the center compared to the edges. This indicates the appearance of a new flow channel. (b) and (c) Grayscale of velocity magnitude (light is higher velocity) before and after the appearance of the new channel. Velocity in (a) is along dashed line near the front of the cell. (d) and (e) Images of the whole cell at the same times with black arrows are for boundary velocity and white arrows are for cytoplasm velocity.

III. FLOW-INDUCED CHANNEL FORMATION

Though the rheology of actin networks is very complex, it is generally accepted that they are shear thinning, which means that the effective viscosity is a decreasing function of the shear rate. In *Physarum* it is observed that when the pressure gradient is low, there is little flow of the cytoplasm, but above a certain pressure, the cytoplasm begins to flow [2,19,21–25]. This suggests that the cytoplasm of *Physarum* can be described as a yield stress fluid. That is, for low stresses the cytoplasm behaves as a solid, but above a critical stress it behaves like a fluid. Such a transition is likely related to the rupture of the cytoskeleton in response to stress. As the material flows, these crosslinks between filaments and the filaments themselves are ruptured, allowing the mixture to flow more easily.

The simple description of the cytoplasm as a yield stress fluid is inadequate to explain flow channel formation. The reasoning is as follows: consider the pressure-driven steady flow between two parallel plates (analogue to Poiseuille flow) of a yield stress fluid. The shear stresses are largest near the walls of the channel, and so the material near the wall liquefies and the middle flows as a solid core [26], which is the exact opposite of what is observed in flow channels of *Physarum* (solid near the walls and liquid in the center).

To describe channel formation in shear thinning actin networks, we must take a different approach than describing the rheology of the material with a single effective stress tensor. We must explicitly account for the dynamics of the networked actin. The two-fluid model [27,28] has been used successfully in the past to describe channel formation in gels [29,30]. In these models the sol and gel are described as separate but interacting fluids, each moving with their own velocity. The local composition of the mixture of sol and gel is described in terms of volume fractions.

In [30] the two-fluid models was applied to describe the internal flow and cytoskeletal organization in *Amoeba Proteus*, which like *Physarum*, is a giant amoeboid cell that migrates using cytoplasmic streaming. In this model the flow channel resulted from chemically elevated contractile stresses near the cell membrane. The flow itself was not involved in signaling the development of channels. In a two-fluid model of channel formation in biofilms [29], the flow was involved in signaling channel formation, but the driving force of channeling was osmotic pressure not fluid stresses. It was assumed that for a range of polymer concentrations, the polymer/solvent mixture was unstable and thus a phase separation instability drove spatial pattern formation. Neither of these previous models provides a satisfactory explanation for the formation flow channels observed in *Physarum*.

In this paper, we propose a model that is similar in spirit to the two-phase flow models, in that we model the cytosol and actin network separately. However, we assume that the network forms and breaks, but does not flow. This reduction is reasonable for stiff networks, and it significantly simplifies the analysis of the model. Below we present the model and show that under very simple assumptions this provides a new explanation for the formation of channels in response to flow.

A. Model

We assume that the actin network is rigid so that it does not move in space. To describe the fluid flow through the network we use the Brinkman equation [31]

$$\mu \Delta \mathbf{u} - \xi \mathbf{u} - \nabla p = 0, \tag{1}$$

$$\nabla \cdot \mathbf{u} = 0, \tag{2}$$

where $\mathbf{u}$ is the fluid velocity, p is the pressure, μ is the fluid viscosity, and ξ is the drag coefficient. The first term in (1) represents the viscous stress in the fluid, and the second term represents the drag force that the network exerts on the fluid. The permeability of the network is the ratio of the drag coefficient to the viscosity μ/ξ. In the absence of viscous stress this model reduces to Darcy's law for flow through a porous medium. Brinkman proposed including the viscous term [31] so that in the limit that ξ goes to zero Stokes

flow is recovered. This model is an appropriate description of viscous flow through low volume fraction suspensions of fibers or particles which have small diameters relative to the pore size [32]; the validity of this model is still under debate at high solid volume fractions [33]. We use the Brinkman equation instead of Darcy's law because within the flow channel the volume fraction of polymer is very low, and the viscous stresses are relevant. As described below, the drag coefficient is a function of polymer concentration. In regions of space where the polymer concentration is not small, the drag term dominates the viscous term, and the model effectively reduces to Darcy's law.

Let θ denote the concentration of networked actin gel, which evolves according to

$$\theta_t = k_+ - k_-(|\mathbf{u}|)\theta. \tag{3}$$

It is assumed that the network forms at a constant rate, but it ruptures at a rate that depends on the local fluid velocity. This is because flow through the polymer network stresses the polymers and crosslinks, which leads to an increase in the degradation rate. We assume that the breaking rate is an exponentially increasing function of the force [34,35]:

$$k_-(|\mathbf{u}|) = k_-^0 \exp(b|\mathbf{u}|), \tag{4}$$

where b is a constant which characterizes how sensitive the breaking rate is to the applied force. In Sec. IV D we show that any function which increases sufficiently rapidly will lead to similar qualitative results. We assume that the drag coefficient is proportional to the concentration of networked actin gel:

$$\xi = \xi_0\theta, \tag{5}$$

where ξ_0 is a proportionality constant.

To investigate channeling we explore the flow profile that develops in a pressure-driven flow between two parallel plates at $y = 0$ and $y = h$. In this situation, the velocity is unidirectional and the velocity profile is only a function of y (see Fig. 4). The velocity profile satisfies the equation

$$\mu u_{yy} - \xi_0\theta u + f = 0, \tag{6}$$

where u is the velocity in the direction perpendicular to the y axis and f is the negative of the pressure gradient, which we refer to as the applied pressure gradient. We assume the no-slip boundary condition on the walls of the plates:

$$u(0) = u(h) = 0. \tag{7}$$

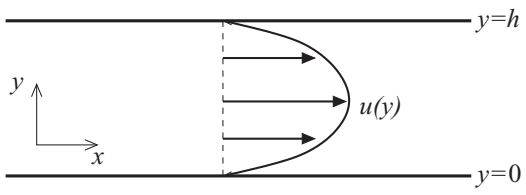

FIG. 4. To investigate channeling we consider the flow between two infinitely long parallel plates located at $y = 0$ and $y = h$ driven by an applied pressure gradient. The flow is unidirectional and the flow profile $u(y)$ is a function of only the height between the two plates.

For a given applied pressure gradient, Eqs. (3)–(7) determine the velocity profile and the concentration of network.

To facilitate the analysis of the model when the network concentration depends on the applied pressure gradient, we nondimensionalize the equations. We scale the velocity by b^{-1}, the network concentration by k_+/k_-^0, time by $1/k_-^0$, and length by h. This gives the dimensionless system of equations

$$\epsilon u_{yy} - \theta u + f = 0, \tag{8}$$

$$\theta_t = 1 - \exp(|u|)\theta, \tag{9}$$

$$u(0) = u(1) = 0. \tag{10}$$

The single dimensionless parameter

$$\epsilon = \frac{\mu}{h^2\xi_0} \tag{11}$$

characterizes the ratio of viscous forces to drag forces and is assumed to be small ($\epsilon \ll 1$). At low flow rates $\exp(|u|) = O(1)$, and the force on the fluid is dominated by the drag term. The parameter ϵ may be interpreted as the ratio of the permeability of the cytoskeleton to the squared height of the channel. The permeability of the cytoskeleton within the lamellipodium of crawling keratocytes has been estimated as 10^{-3} μm^2 [36], and the thickness of the microplasmodia considered in this paper are on the scale of 10 μm. These values give an estimate of $\epsilon = 10^{-5}$.

We analyze how the velocity profile changes as a function of the applied pressure gradient f. We treat f as a given constant and solve for the steady state velocity profile. In this case, Eqs. (8)–(10) reduce to

$$\epsilon u_{yy} - \exp(-|u|)u + f = 0, \tag{12}$$

with boundary conditions (10). Before proceeding, we comment on the biological relevance of investigating a flow driven by a constant pressure gradient. During shuttle streaming in *Physarum* the pressure gradient oscillates in time. The time scale of this oscillation is faster than the time scale of the turnover of the cytoskeleton [2]. In the Appendix we use averaging to show that Eq. (12) describes the steady state spatially dependent amplitude of the velocity oscillation and that the constant f is related to the amplitude of the pressure oscillation.

B. Numerical results

Depending on the values of ϵ and f, Eq. (12) may have multiple solutions. We find the solutions by advancing the time dependent problem (8)–(10) to steady state. To generate the solutions for the interval $f \in [0, f_{\max}]$, we begin at $f = 0$ for which the solution is $u = 0$. We update f incrementally and solve to steady state using the solution at the previous value of f as an initial condition. When $f_{\max}$ is reached, we repeat this process by decreasing f back to 0 to find a possible second set of solutions. This gives a set of dynamically stable solutions. When there are multiple solutions, we use Newton's method to solve for the unstable solutions by taking initial guesses in between the two stable solutions. This method fails to converge when ϵ is very small. We use $\epsilon = 5 \times 10^{-4}$

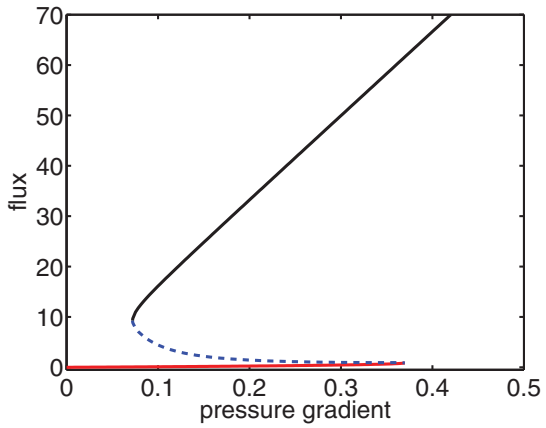

FIG. 5. (Color online) Flux as a function of applied pressure gradient where the velocity profile satisfies Eq. (12). The value of ϵ is 5×10^{-4}. The unstable solution is represented by a dashed line.

to facilitate the numerical computations, and the effect of changing ϵ is considered later.

In Fig. 5 we show the flux as a function of the applied pressure gradient for $\epsilon = 5 \times 10^{-4}$. The flux through a cross section of the domain is

$$Q = \int_0^1 u \, dy. \tag{13}$$

For low and high pressure gradients there is one solution, but for a range of pressure gradients in between there are three solutions. The upper and lower branches correspond to the dynamically stable solutions, and the middle branch corresponds to the unstable solution. Beginning at a low pressure gradient, there is little flow through the domain, but once the gradient exceeds a critical value the flux jumps suddenly by about a factor of 70. This solution will stay in this high-flux state until the pressure gradient drops below a critical value. Although quantitatively different, the solutions for other small values of ϵ have similar characteristics.

In Fig. 6 we show the three velocity profiles and network concentration profiles for $f = 0.20$. We refer to these three solutions as the lower, middle, and upper branch solutions corresponding to the sizes of their respective fluxes. The three solutions have very different characters. The lower branch solution is a plug flow, which means that the drag dominates through most of the domain except near the boundary. This solution resembles flow through a porous medium. The upper branch solution resembles a Poiseuille flow. Comparing with the gel profiles, we see that for this fast flow there is almost no gel throughout the domain, and so the drag term is negligible. The middle branch solution is the most interesting. There is a flow channel in the middle of the domain where there is little gel and the flow is much faster than near the edges. Unlike the upper branch solution, there remains a significant amount of gel in a nonvanishing region near the walls.

This simple model of a network which ruptures in response to flow reproduces the phenomenon of a critical pressure below which there is little flow. When the critical pressure is reached the gel does not produce a flow channel in the middle of the domain. Instead the gel is broken up throughout the entire domain. Although there are channeled solutions, they are unstable and would thus not be observable.

C. Relieving the pressure

In *Physarum*, the pressure gradient driving the flow is generated by a spatial gradient in the cortical contraction stress. If the internal gel rearranges or ruptures, this provides less resistance to flow and should reduce the pressure applied to the remaining internal gel. This effect is not captured by the model described in the previous sections. The assumption of the previous model is that the domain is infinitely long and the flow is driven by a constant pressure gradient. In this section we adapt the previous model so that when the flux through the domain increases, the pressure applied is reduced.

We again consider pressure-driven flow through parallel plates, but we do not treat the domain as infinitely long. The domain is divided into three segments: an upstream region, a downstream region, and a middle region. In this model we describe the flow through the middle region. Suppose that the middle region is sufficiently long that the flow is fully

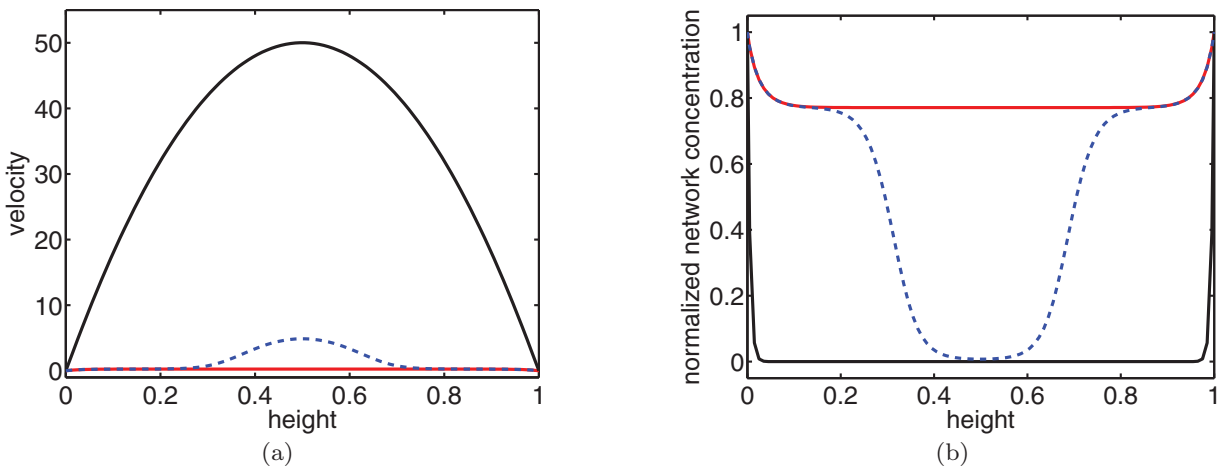

FIG. 6. (Color online) Solutions to Eq. (12) for $\epsilon = 5 \times 10^{-4}$ at $f = 0.20$. The unstable solution is represented by a dashed line. (a) Velocity profiles. (b) Normalized network concentration.

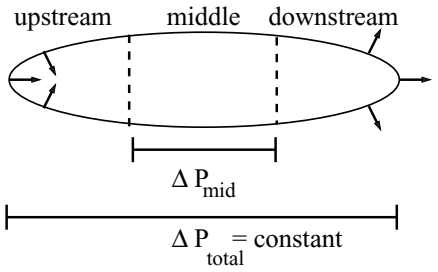

FIG. 7. The pressure drop across the entire physical domain is a given constant, but the effective pressure drop across the middle segment depends on the flow.

developed, and so that it can be described by a one-dimensional model. The pressure drop across the whole domain is a given constant. This pressure, for example, is generated by the contraction of the organism at one end and relaxation at the other. The pressure drop over the middle region is no longer constant, but it can be computed from the total pressure drop and the flow (see Fig. 7).

Suppose that in each segment the flux through and pressure drop across the segment indexed by i are related by

$$\Delta P_i = R_i Q_i, \tag{14}$$

where ΔP_i is the pressure drop, R_i characterizes the resistance, and Q_i is the flux. The total pressure drop across the entire domain is just the sum of the pressure drops across each segment

$$\Delta P_{\text{total}} = \Delta P_{\text{up}} + \Delta P_{\text{mid}} + \Delta P_{\text{down}}. \tag{15}$$

Because the fluid is incompressible, the flux through each segment is equal, $Q = Q_i$. Putting these equations together, the pressure drop across the middle of the domain is

$$\Delta P_{\text{mid}} = \Delta P_{\text{total}} - (R_{\text{up}} + R_{\text{down}})Q. \tag{16}$$

We assume that the resistances in the upstream and downstream regions are constant. Therefore the effective pressure drop across the middle segment is a linear function of the total applied pressure drop and the flux. This simple description has the desired property that if the resistance to flow in the middle segment goes down, the flux will go up, which will relieve some pressure and cause a decrease in the effective pressure gradient.

To adapt the model from the previous section, we modify (12) so that the effective pressure gradient decreases linearly as the flux increases. The equation we study is

$$\epsilon u_{yy} - \exp(-|u|)u + f - \delta Q = 0, \tag{17}$$

where the flux Q is defined by Eq. (13). The parameter δ characterizes the total resistance to flow of the upstream and downstream regions. The value of f is related to the size of the pressure gradient applied to the entire domain, and $f - \delta Q$ is the effective pressure gradient on the region being modeled (i.e., the middle region).

We repeat the computations of the previous section for this new model which incorporates pressure relief. In Fig. 8 we show the flux as a function of the applied pressure gradient for $\delta = 0.1$ and again $\epsilon = 5 \times 10^{-4}$. As before there is one

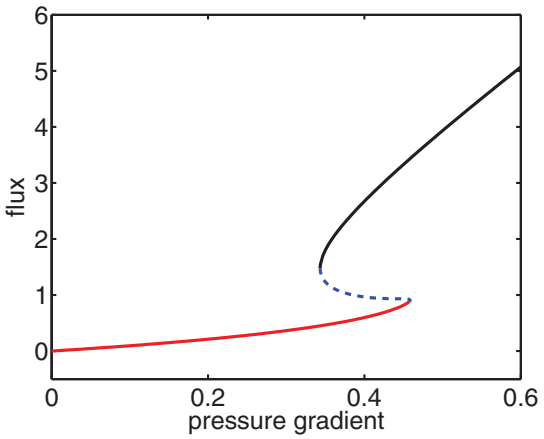

FIG. 8. (Color online) Flux as a function of applied pressure gradient, where the velocity profile satisfies Eq. (17) which includes the effect of pressure relief. The value of ϵ is 5×10^{-4} and the value of δ is 0.1. The unstable solution is represented by a dashed line.

solution at low and high pressure gradients, and there is a range for which there are three solutions. The solutions on the upper and lower branches are stable, and the solution on the middle branch is unstable.

In Fig. 9 we show the three velocity profiles and network concentration profiles for $f = 0.40$. As before, the lower branch solution is a plug flow and the gel is uniform across the middle of the domain. The other two solutions both correspond to flow channels. There is a region in the middle of the domain in which the gel concentration is much smaller than near the edges. This feature is more pronounced on the upper branch solution in which there is almost no gel in the middle of the domain. The velocity profile is almost parabolic in the flow channel and relatively flat in the region of high gel concentration. Unlike the model on the infinite domain, this finite domain model which includes the effect of pressure relief produces dynamically stable channeled solutions.

D. PARAMETERS

There are only two parameters to this model problem: ϵ is the ratio to viscous force to drag force and δ is the parameter which characterizes the resistance to flow in the upstream and downstream regions. In this section we explore the effects to these two parameters on the observations in the previous sections.

In the previous section we only showed the flux versus pressure gradient curve for a single value of δ. Here we show that solutions for any value of δ can be obtained from the solutions for $\delta = 0$. Let $u(y; f,\delta)$ be a solution to (17) for given values of δ and f. The solution for any value of δ is related to the solution for $\delta = 0$ by

$$u(y; f,0) = u(y; f + \delta Q,\delta). \tag{18}$$

Thus the solutions for $\delta = 0$ can be mapped to the solutions for any value of δ. This is illustrated in Fig. 10. Increasing δ has two effects. First, the range of pressure gradients where there are stable channeled solutions increases, and second the range of pressure gradients where there are multiple solutions decreases.

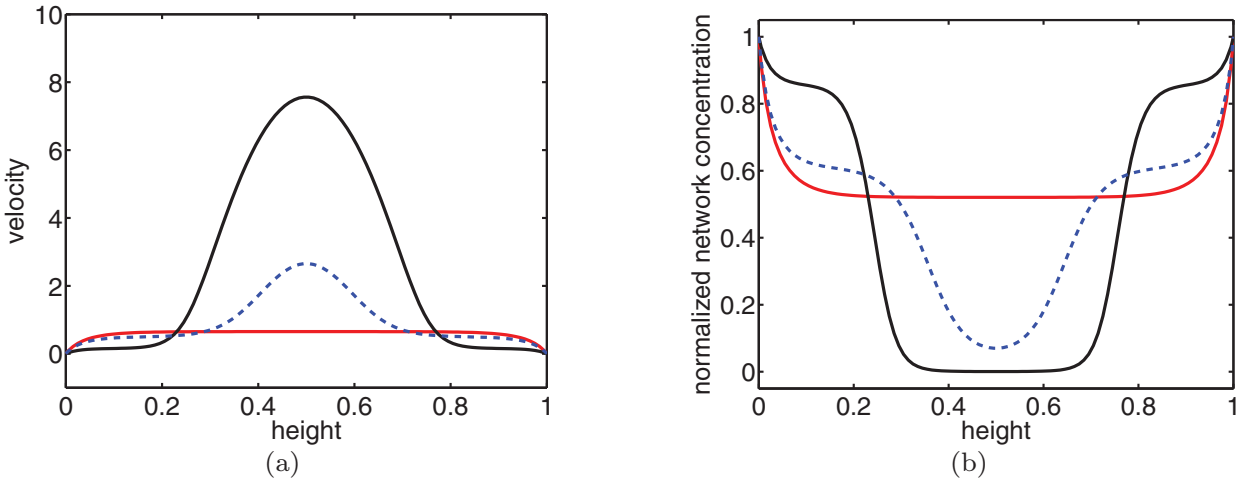

FIG. 9. (Color online) Solutions to Eq. (17) for $\epsilon = 5 \times 10^{-4}$ and $\delta = 0.1$ at $f = 0.40$. The unstable solution is represented by a dashed line. (a) Velocity profiles. (b) Normalized network concentration.

Next we consider the effect of changing ϵ. We have assumed that the drag forces dominate over the viscous forces when the internal gel is intact, which means that $\epsilon \ll 1$. In Fig. 11 we plot the flux versus applied pressure gradient for different values of ϵ for $\delta = 0$. This graph shows that for ϵ large enough the curve becomes single valued, which means there is only one velocity profile for a given pressure gradient. With $\delta = 0$ the channeled solutions correspond to the unstable middle branch of solutions. Thus we conclude that ϵ must be small for the model to show channeling.

IV. ASYMPTOTIC ANALYSIS

In this section we explore the solutions to (12) further using asymptotic analysis in order to explain some of the features of the solutions which were demonstrated numerically. As we showed in the previous section, the solutions for $\delta = 0$ can be mapped to give solutions for nonzero δ. Therefore it is sufficient to analyze the case $\delta = 0$ to understand the nature of the solutions. By examining the limit of $\epsilon \to 0$, we give expressions for the two stable solutions, we calculate the critical values of f at the bifurcation points, and we compute the maximum value of the velocity in the channeled solutions. This analysis leads to general conditions on the breaking rate which are sufficient to exhibit channeled solutions.

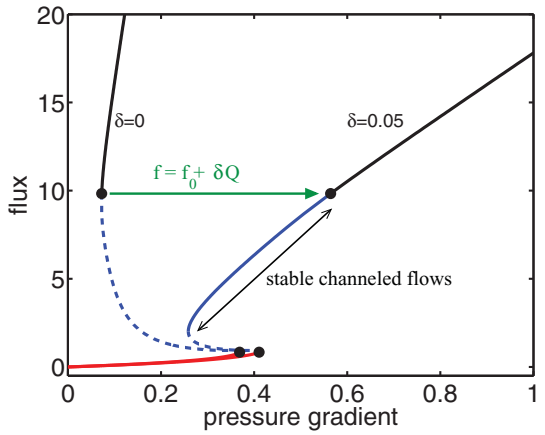

FIG. 10. (Color online) Flux vs applied pressure gradient for $\epsilon = 5 \times 10^{-4}$ for $\delta = 0$ and $\delta = 0.05$. The curve for nonzero values of δ can be obtained from the curve for $\delta = 0$. As δ increases more channeled solutions become stable and the range of pressure gradients where there are multiple solutions decreases.

A. Plug flow: lower branch

For small values of f the only solution is a plug flow. This solution resembles that of flow through a porous medium, in which the velocity is proportional to the pressure gradient. In our model problem, this corresponds to the case when the drag forces dominate the viscous forces. The value of the fluid velocity away from the boundary is found by taking the limit as $\epsilon \to 0$ in (12) which gives

$$-u \exp(-u) + f = 0, \tag{19}$$

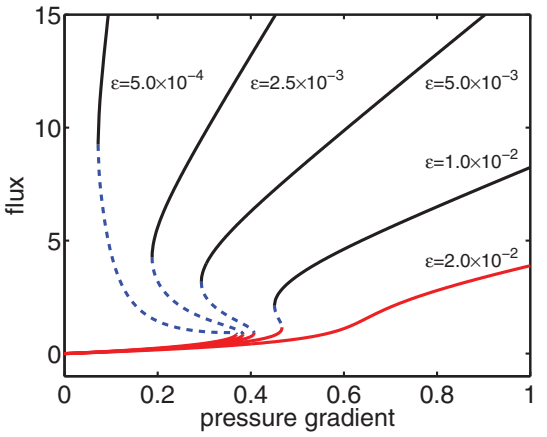

FIG. 11. (Color online) Flux vs pressure gradient for different values of ϵ with $\delta = 0$. For large enough ϵ there are no channeled solutions.

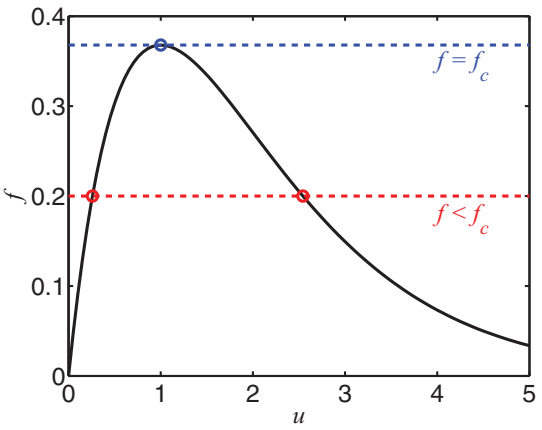

FIG. 12. (Color online) For $f < f_c = \exp(-1)$ Eq. (19) has two solutions, and for $f > f_c$ there is no solution.

where it is assumed that $f > 0$ and so $u > 0$. From this simple equation we can compute the maximum value of f for which a plug flow exists. That is, the value of f above which only the upper branch solution exists.

The function $f = u\exp(-u)$ is plotted as a function of u in Fig. 12. For small values of f (19) has two solutions, and for large values of f there is no solution. The boundary between these two regions occurs at the critical value of $f_c = \exp(-1)$, which corresponds to $u = 1$. Notice that in Fig. 5 the lower branch ends at approximately $f_c = \exp(-1) \approx 0.368$. Therefore to leading order in ϵ the value f_c represents the critical applied pressure gradient, above which the gel falls apart and the plug flow solution disappears.

For $f < f_c$ there are two solutions to Eq. (19). The smaller of the two solutions goes to 0 as f goes to zero, while the larger one goes off to infinity. Thus we observed the smaller solution in the numerical simulation. We will show in Sec. IV C that only the smaller plug flow solution is possible because of the boundary conditions. To find an asymptotic expression for the velocity, we exploit that there are two small parameters ϵ and f. The solution to (19) for small f is

$$u = f + f^2 + O(f^3). \tag{20}$$

This solution is a valid approximation to the solution of (12) away from the boundaries, but near the boundary the viscous term cannot be ignored.

There is a boundary layer of thickness $O(\epsilon^{1/2})$ in which the velocity transitions sharply to satisfy the boundary conditions. We rescale the spatial variable by $Y = \epsilon^{-1/2}y$, and define $U(Y) = u(y)$ to get the equation in the boundary layer at $y = 0$ as

$$U_{YY} - U\exp(-U) + f = 0, \tag{21}$$

$$U(0) = 0. \tag{22}$$

We find solutions to this equation by again exploiting that f is small and expanding the drag term in powers of f. The two-term expansion that satisfies the boundary condition and the matching condition

$$\lim_{Y\to\infty} U(Y) = \lim_{y\to 0^+} u(y) \tag{23}$$

is

$$U(Y) = [(1 - \exp(-Y)] + [3 - (2 + 3Y)\exp(-Y) + \exp(-2Y)]\frac{f^2}{3} + O(f^3). \tag{24}$$

There is a similar boundary layer at $y = 1$. In Fig. 13(a) we show the numerical solution to (12) compared with the two-term (in f) asymptotic solution for $f = 0.1$ and $\epsilon = 5 \times 10^{-4}$. We see that this is a uniform approximation to the solution throughout the domain. We compute the maximum error in this approximation to be less than 2%.

B. Parabolic flow: upper branch

On the upper branch the gel has essentially fallen apart and the solution appears to be parabolic. When the velocity is large the drag term is exponentially small, and so there is effectively

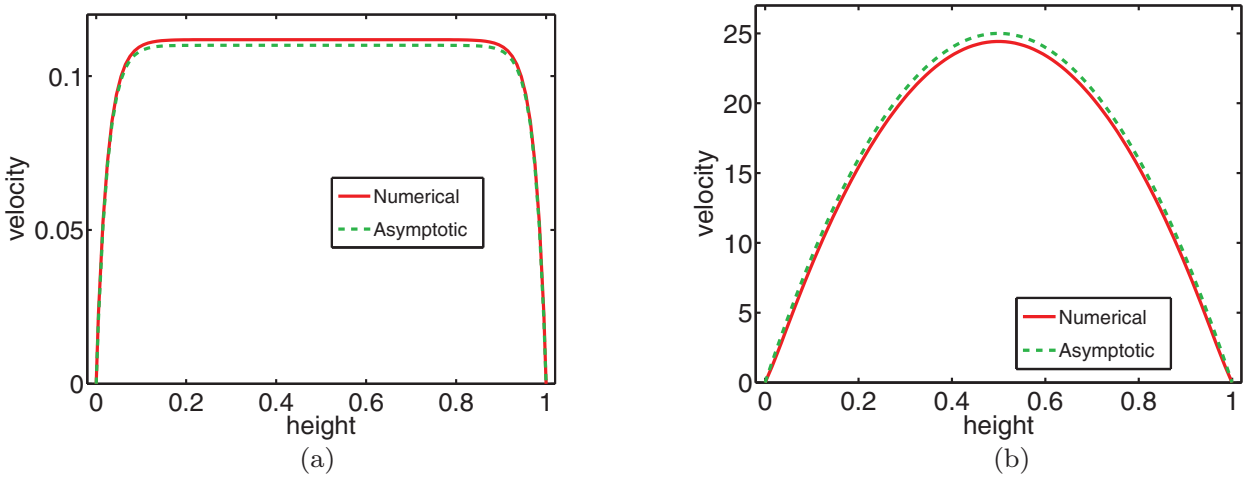

FIG. 13. (Color online) Comparison of the numerical solution to Eq. (12) and the asymptotic solution (a) on the lower branch in the plug flow regime and (b) on the upper branch in the parabolic flow regime for $f = 0.1$ and $\epsilon = 5 \times 10^{-4}$. The error in the asymptotic approximation is around 2% in both cases.

no drag in the middle of the domain. Near the boundaries the velocity is not large but the drag term is still small in this region because the velocity is small.

Ignoring the drag throughout the domain, the leading order solution to (12) is

$$u = \frac{f}{2\epsilon}\, y(1-y). \tag{25}$$

In Fig. 13(b) we compare this asymptotic solution with the numerical solution for $f = 0.1$ and $\epsilon = 5 \times 10^{-4}$. The approximation is uniformly valid throughout the domain, and for these parameters the error is less than 2.3% everywhere.

We have explained the form of the solution on the upper and lower branches and estimated the value of the pressure gradient at which the lower branch disappears. It is not obvious what happens when the upper branch disappears and what determines the shape of the channeled solution. These are explained in the next section.

C. Phase plane

Equation (12) is equivalent to the first-order system

$$u_y = v, \tag{26}$$

$$\epsilon v_y = u\exp(-u) - f, \tag{27}$$

where we have assumed that $u > 0$. For $f < \exp(-1)$, there are two equilibrium points which are the roots of Eq. (19). Denote these two roots by u_- and u_+, where $u_- < 1 < u_+$. It is straightforward to show than u_- is a saddle point and u_+ is a center.

After multiplying Eq. (12) by u_y we obtain

$$\frac{d}{dy}\left[\frac{\epsilon}{2}(u_y)^2 + (u+1)\exp(-u) + uf\right] = 0. \tag{28}$$

Thus the "energy" function

$$\mathcal{E} = \frac{\epsilon}{2}v^2 + (u+1)\exp(-u) + uf \tag{29}$$

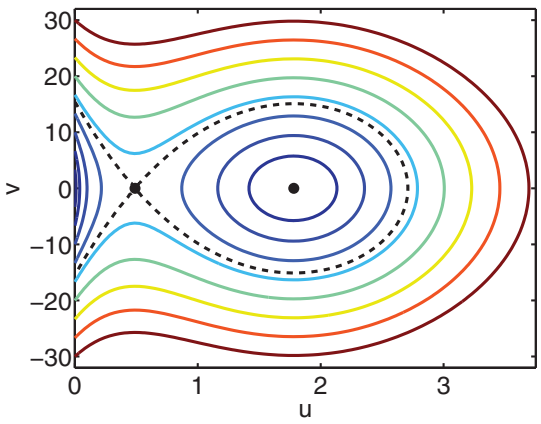

FIG. 14. (Color online) Level sets (not equally spaced) of the energy function (29) which correspond to solutions of the system (26) and (27). The two equilibrium points are marked with dots. The stable and unstable manifolds of the smaller equilibrium point are plotted by the dashed curve. There is a homoclinic orbit which encircles the larger equilibrium point. The parameters are $f = 0.30$ and $\epsilon = 5 \times 10^{-4}$.

is constant on the trajectories of (26) and (27), or equivalently the level sets of $\mathcal{E}$ are the trajectories in the phase plane. In Fig. 14 we show the location of the two equilibrium points and some sample trajectories for $f = 0.30$ and $\epsilon = 5 \times 10^{-4}$. Note this is in the parameter range where there are three solutions to the boundary value problem (12). The stable and unstable manifolds of the saddle point are plotted with a dashed curve. There is a homoclinic orbit encircling the other equilibrium point.

Only the trajectories that satisfy the boundary conditions $u(0) = u(1)$ are solutions to the original boundary value problem (12). We can now explain why there is only one plug flow solution despite the fact that there are two roots of (19). In the phase plane, the larger solution u_+ is separated from the $u = 0$ line by the homoclinic orbit. For the boundary value problem this means that there is no boundary layer capable of matching the outer solution $u = u_+$.

Whenever there are two equilibrium points, that is, when $f < \exp(-1)$, the phase plane has the same qualitative structure. At $f = \exp(-1)$ the two equilibrium points come together. As discussed previously, this is the point at which the plug flow solution and channeled solution come together. What remains to be explained is what happens at the point where the parabolic solution and channeled come together. To understand this transition, we must understand the structure of the channeled solution.

In Fig. 15(a) we show the plug flow solution and the channeled solution for $f = 0.30$ and $\epsilon = 10^{-3}$, and in Fig. 15(b) we show the same solutions in the phase plane along with the equilibrium points and stable and unstable manifolds of the saddle point. The boundary layer near $y = 0$ closely follows the stable manifold, and the layer near $y = 1$ closely follows the unstable manifold. The channeled solution has similar boundary layers, except that it follows these manifolds on the other side. The channeled portion of the solution closely follows the homoclinic orbit on the outside. It is difficult to see the difference between the different trajectories on this scale, and so in Fig. 15(c) we show a closeup around the saddle point.

The value of ϵ only changes the scale of the vertical axis in the phase plane. The shape of the trajectories of (26) and (27) does not depend on ϵ. The value of ϵ determines which trajectories in the phase plane are solutions to the boundary value problem. By rescaling the spatial variable in (12) by

$$y = \epsilon^{1/2}\hat{y}, \tag{30}$$

the boundary value problem becomes

$$u_{\hat{y}\hat{y}} - \exp(-|u|)u + f = 0; \quad u(0) = u(\epsilon^{-1/2}) = 0. \tag{31}$$

The phase plane trajectories that satisfy this boundary value problem are those that begin at $u = 0$ and return to $u = 0$ by "time" $\epsilon^{-1/2}$. Thus as ϵ goes to zero the time to traverse these trajectories goes to infinity. The only trajectories that meet this requirement and remain bounded are those that closely follow the trajectories in and out of the saddle point.

As f gets smaller there are no topological changes in the phase plane. As f goes to zero the saddle point goes to zero, and the other equilibrium point (the center) goes off to infinity. Because the homoclinic orbit surrounds the larger equilibrium point, the homoclinic gets infinitely large. This explains why

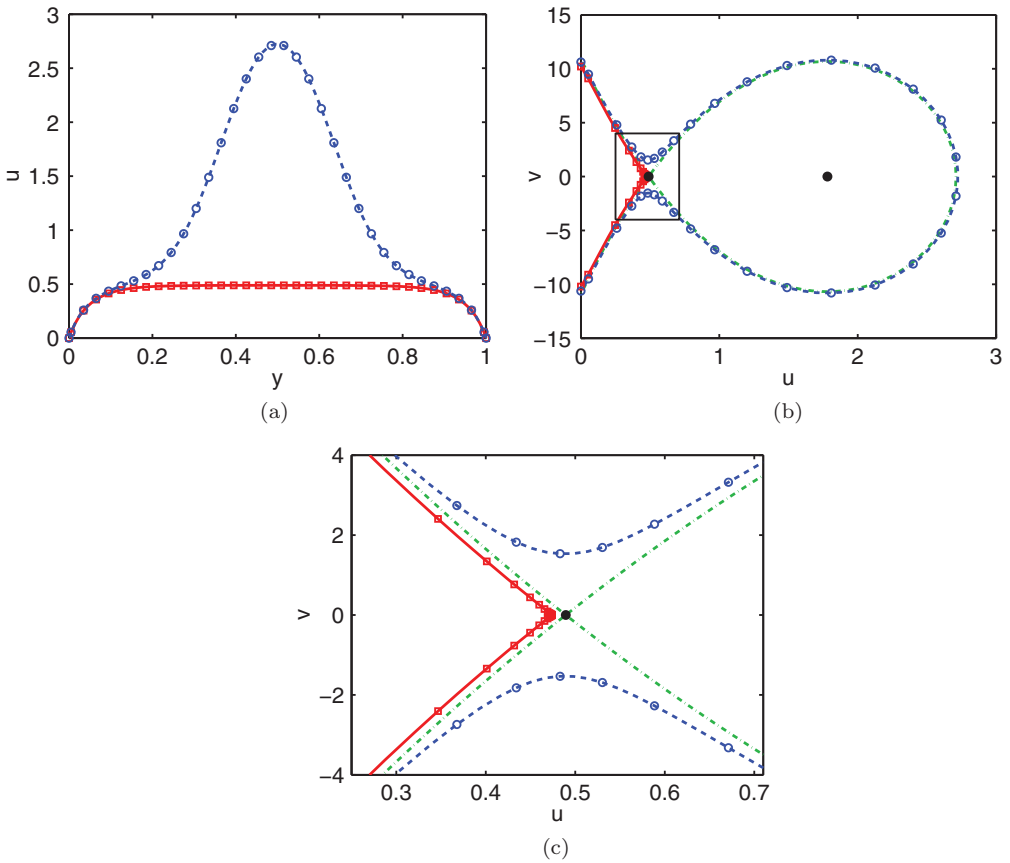

FIG. 15. (Color online) (a) Plug flow solution (red squares) and channeled solution (blue circles) for $f = 0.30$ and $\epsilon = 10^{-3}$. (b) Solutions plotted in the phase plane along with the equilibrium points and the stable and unstable manifolds of the saddle point (green dash-dot curve). (c) Closeup of the solutions around the saddle point.

the channeled solution and parabolic solution merge for small f. The channeled solution becomes larger while the parabolic solution gets smaller.

The homoclinic orbit intersects the u axis in two places: at the saddle point u_- and at the maximum extent of the homoclinic orbit, which gives the maximum velocity of the flow in the channeled solution. Because these two points are on the same trajectory, they have the same energy, and so the maximum velocity of the channeled solution can be found by solving the equation

$$(u+1)\exp(-u) + fu = (u_- + 1)\exp(-u_-) + fu_- \qquad (32)$$

for u. By exploiting that f is small and u is large, we find that the leading order solution to this equation is

$$u = f^{-1}. \qquad (33)$$

From (25) the maximum velocity of the parabolic solution is

$$u = \frac{f}{8\epsilon}. \qquad (34)$$

To find the value of f at which the channeled solution meets the parabolic solution, we equate these two velocities to find that

$$f = \sqrt{8\epsilon}. \qquad (35)$$

From the asymptotic analysis we construct a bifurcation diagram of maximum velocity versus pressure gradient. The lower branch corresponds to the drag dominated solution, and the maximum velocity is the smaller root of (19). The upper branch corresponds to the viscous dominated case, and the maximum velocity is given by (34). The middle branch corresponds to the channeled solution, and it is neither drag dominated nor viscous dominated. It exists for pressure gradients in the range $\sqrt{8\epsilon} < f < \exp(-1)$ and its maximum velocity is the nontrivial solution of (32). In Fig. 16 we show plots of the maximum velocity versus the pressure gradient for both the leading order asymptotic solution for the numerical solution of the boundary value problem. When these two plots are superimposed, the only notable difference is at the left knee. Elsewhere, the curves are indistinguishable to the eye on this scale. The similarity between these two plots validates our asymptotic analysis.

D. Generalization

To this point we have assumed that the breaking rate of the gel is the exponentially increasing function (4). The analysis of the previous section gives insight into what breaking rate functions give channeling behavior. We consider the equation

$$\epsilon u_{yy} - g(u) + f = 0, \qquad (36)$$

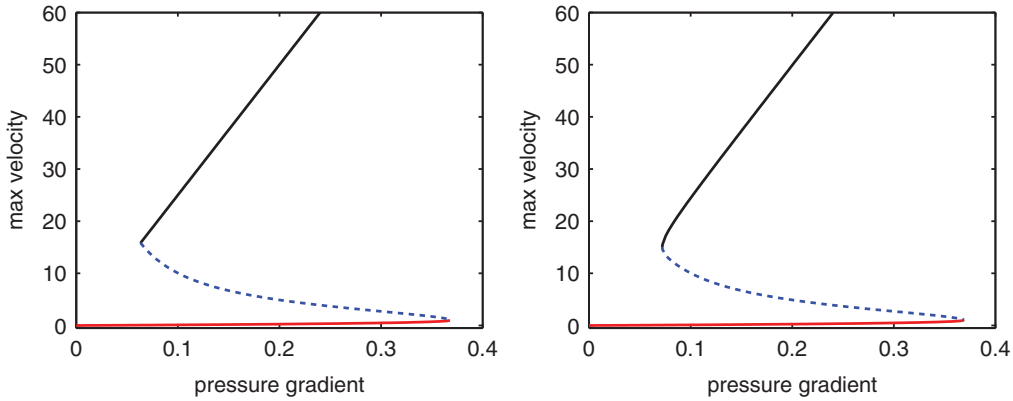

(a) Asymptotic (b) Numerical

FIG. 16. (Color online) Plots of maximum velocity vs pressure gradient for $\epsilon = 5 \times 10^{-4}$. (a) Asymptotic solution. (b) Numerical solution of the boundary value problem.

where the drag term g is proportional to $u/k_-(|u|)$. For simplicity we assume that $u > 0$ so that we ignore the absolute value. As before, we examine the first-order system

$$u_y = v, \tag{37}$$

$$\epsilon v_y = g(u) - f. \tag{38}$$

Sufficient conditions for obtaining channeled solution are

(1) $g(u) = f$ has two roots $u_- < u_+$ when $0 < f < f_c \leqslant \infty$.
(2) $g'(u_-) > 0$ and $g'(u_+) < 0$.
(3) $fu_- - G(u_-) = fu - G(u)$ has a nontrivial root $u_{++} > u_-$, where G is an antiderivative of g.
(4) ϵ is sufficiently small.

The first condition ensures that there are two equilibrium points for a range of applied pressure gradients. The second condition ensures that the smaller equilibrium is a saddle point and the larger equilibrium point is a center. The third condition means that the level curve of the energy function containing u_- intersects the u axis at a second point, which implies that there is a homoclinic orbit. The final condition ensures that a trajectory which follows the outside of the homoclinic orbit is a solution to the boundary value problem.

These conditions translate into very mild conditions on the form of the breaking rate function. For example, if the breaking rate is a strictly positive, increasing function which grows faster than linear, the model will exhibit channeling for small enough ϵ. Mathematically these conditions are (1) $k_-(0) > 0$, $k'_-(|u|) > 0$, and $k_-(|u|)/u \to \infty$ as $u \to \infty$. These imply that the function g above satisfies $g(0) = 0$, $g'(0) > 0$, and $g \to 0$ as $u \to \infty$. The first two conditions on g for channeling are clearly satisfied. The only nontrivial condition to check is that there is a homoclinic cycle, that is, the third condition on g. This is argued below.

Assume that f is in the range where the first two conditions on g are met. Let $W(u) = fu - G(u) - E_-$, where $E_- = fu_- - G(u_-)$. The function W has a root at u_-, and to guarantee a homoclinic orbit we need that W has another root larger than u_-. The first two derivatives of W are $W'(u) = f - g(u)$ and $W''(u) = -g'(u)$. Because u_- is an equilibrium point, $W'(u_-) = 0$, and because $g'(u_-) > 0$, $W''(u_-) < 0$. Thus W is negative for some values of u to the right of u_-. Because $g \to 0$ as $u \to \infty$, $W'(u) \to f$, and so $W(u) \to \infty$. Therefore there is a second root to W, which means that there is a homoclinic orbit.

V. DISCUSSION

The model we present here provides a novel and simple explanation for flow-induced channel formation in the cytoplasm of *Physarum*. As our asymptotic analysis shows, the qualitative predictions of the model are not sensitive to our assumptions. An important feature of the solutions is the hysteresis of flow channel formation. In our model exploration we only analyzed the steady state solutions, but in the cell, the pressure is oscillating temporally. Thus the flow speed is constantly changing, and the robustness of a hysteric switch is needed to maintain the channels under these conditions. We expect that models with more detailed treatments of the rheology and actin dynamics would produce similar results as long as fluid stresses increase the rupture rate in the cytoskeleton.

The forces involved in cell locomotion are all generated locally, but they must be coordinated across different regions of the cell in order to achieve directed motion. Channel formation is one means of providing global coordination across the cell. *Physarum* is an unique cell given its large size and extremely fast flows, but the coupled dynamics of cytoplasmic streaming and cytoskeleton are involved in the locomotion of many other cells [37,38]. Understanding how local stimulus is translated into behavior is a fundamental question. *Physarum* has been shown to exhibit fascinating global behavior such as finding optimal solutions through mazes [12,13], which we interpret as a form of primitive intelligence. The physics of soft matter of cytoplasm is a key component of how the cell processes information to achieve such complex tasks [10].

ACKNOWLEDGMENTS

The authors would like to thank Kenji Matsumoto for performing the particle image velocimetry analysis in the experiments, as well as Joseph Biello, James Keener, and Tim Lewis for helpful discussions related to the asymptotic analysis. The work of RG was supported in part by NSF-DMS

Grant No. 0540779 and by UCOP Grant No. 09-LR-03-116724-GUYR; the work of TN was supported in part by JSPS KAKENHI No. 20300105, Human Frontier Science Program Grant No. RGP51/2007, and JST CREST "Alliance for breakthrough between mathematics and sciences"; the work of GW was supported in part by NSF-DMS Grants No. 0540779 and No. 0934581.

APPENDIX: TIME AVERAGING OSCILLATORY PRESSURES

In this paper we analyzed the velocity and network profiles that result from a constant applied pressure gradient. In *Physarum* the pressure gradient oscillates in time, which drives the flow back and forth. In this Appendix, we show that the velocity profiles of the constant pressure gradient case are related to the amplitude of the oscillating velocity profiles.

Suppose that the applied pressure gradient f in (8) is a periodic function of time with mean zero. The two time scales of the problem are the time scale of cytoskeletal rearrangement and the time scale of the pressure oscillation. The time scale of the oscillation is smaller than the time scale of cytoskeletal rearrangement [2]. We denote the nondimensional period of the pressure oscillation as η, and because time has been scaled by the cytoskeletal rearrangement time $\eta \ll 1$.

To determine the long-time behavior of the model, we use the method of multiple time scales. Let $\tau = t/\eta$ represent the time variable of the fast pressure oscillation scale. We treat the velocity and network concentrations as functions of y, t, and τ, but the applied pressure gradient is a function of only τ. With the two time scales, Eqs. (8) and (9) are

$$\epsilon u_{yy} - \theta u + f(\tau) = 0, \tag{A1}$$

$$\theta_t + \eta^{-1}\theta_\tau = 1 - \exp(|u|)\theta, \tag{A2}$$

along with the boundary conditions (10).

We exploit that $\eta \ll 1$ and expand the solution in powers of η:

$$u = u^0 + \eta u^1 + O(\eta^2), \tag{A3}$$

$$\theta = \theta^0 + \eta\theta^1 + O(\eta^2). \tag{A4}$$

To leading order the network equation is

$$\theta^0_\tau = 0. \tag{A5}$$

Thus, θ^0 does not vary on the fast time scale. The leading order equation for the velocity profile is

$$\epsilon u^0_{yy} - \theta^0(y,t)u^0 + f(\tau) = 0. \tag{A6}$$

Let $f(\tau)$ be expressed as

$$f(\tau) = f_0\hat{f}(\tau), \tag{A7}$$

where

$$\int_0^1 |\hat{f}(\tau)|\, d\tau = 1. \tag{A8}$$

The solution to (A6) is of the form

$$u(y,t,\tau) = U(y,t)\hat{f}(\tau), \tag{A9}$$

where U satisfies the equation

$$\epsilon U_{yy} - \theta^0 U + f_0 = 0. \tag{A10}$$

To determine the equation for θ^0, we use the equation for θ at order η:

$$\theta^1_\tau = -\theta^0_t + 1 - \exp(|u^0|)\theta^0. \tag{A11}$$

To avoid secular growth, the right side of this equation must have zero average over one period of the fast time scale. That is,

$$\int_0^1 \left[-\theta^0_t + 1 - \exp(|u^0|)\theta^0 \right] d\tau = 0. \tag{A12}$$

Using (A5) and (A9), this gives the equation for the network to leading order as

$$\theta^0_t = 1 - \theta^0 \int_0^1 \exp[|U(y,t)\hat{f}(\tau)|] d\tau. \tag{A13}$$

We make the approximation that

$$\int_0^1 \exp[|U(y,t)\hat{f}(\tau)|] d\tau \approx \exp(|U(y,t)|), \tag{A14}$$

which is valid for small amplitude oscillations. The equations for the leading order solution are

$$\epsilon U_{yy} - \theta^0 U + f_0 = 0, \tag{A15}$$

$$\theta^0_t = 1 - \exp(|U|)\theta^0, \tag{A16}$$

which are equivalent to Eqs. (8) and (9).

[1] N. Kamiya, *Protoplasmic Streaming*, Protoplasmatologia, Vol. 8 (Springer, Berlin, 1959).
[2] D. Kessler, in *Cell Biology of Physarum and Didymium*, edited by H. C. Aldrich and J. W. Daniel (Academic, New York, 1982), pp. 145–196.
[3] T. Ueda, Phase Transitions **45**, 93 (1993).
[4] E. B. Ridgway and A. C. H. Durham, J. Cell Biol. **69**, 223 (1976).
[5] Y. Yoshimoto, F. Matsumura, and N. Kamiya, Cell Motil. **1**, 433 (1981).
[6] Y. Yoshimoto, T. Sakai, and N. Kamiya, Protoplasma **109**, 159 (1981).
[7] S. Nakamura, Y. Yoshimoto, and N. Kamiya, Proc. Jpn. Acad. **58**, 270 (1982).
[8] S. Ogihara, Exp. Cell Res. **138**, 377 (1982).
[9] S. Nakamura and N. Kamiya, Cell Struct. Funct. **10**, 173 (1985).
[10] T. Nakagaki and R. D. Guy, Soft Matter **4**, 57 (2008).
[11] T. Nakagaki, H. Yamada, and T. Ueda, Biophys. Chem. **84**, 195 (2000).
[12] T. Nakagaki, H. Yamada, and Á. Tóth, Nature (London) **407**, 470 (2000).
[13] T. Nakagaki, Res. Microbiol. **152**, 767 (2001).

[14] T. Nakagaki, M. Iima, T. Ueda, Y. Nishiura, T. Saigusa, A. Tero, R. Kobayashi, and K. Showalter, Phys. Rev. Lett. **99**, 068104 (2007).
[15] T. Saigusa, A. Tero, T. Nakagaki, and Y. Kuramoto, Phys. Rev. Lett. **100**, 018101 (2008).
[16] A. Tero, S. Takagi, T. Saigusa, K. Ito, D. P. Bebber, M. D. Fricker, K. Yumiki, R. Kobayashi, and T. Nakagaki, Science **327**, 439 (2010).
[17] A. Tero, R. Kobayashi, and T. Nakagaki, J. Theor. Biol. **244**, 553 (2007).
[18] T. Nakagaki, A. Tero, R. Kobayashi, I. Onishi, and T. Miyaji, New Generat. Comput. **27**, 57 (2008).
[19] S. Koya and T. Ueda, ACH, Models Chem. **135**, 297 (1998).
[20] K. Matsumoto, S. Takagi, and T. Nakagaki, Biophys. J. **94**, 2492 (2007).
[21] K. Maruyama, M. Kaibara, and E. Fukada, Biochim. Biophys. Acta **371**, 20 (1974).
[22] S. Hatano and H. Sugino, Protein Nucleic Acid Enzyme **28**, 329 (1983).
[23] R. E. Buxbaum, T. Dennerll, S. Weiss, and S. R. Heidemann, Science **235**, 1511 (1987).
[24] T. Pollar and J. Cooper, Annu. Rev. Biochem. **55**, 987 (1986).
[25] A. Clark and S. Ross-Murphy, in *Biopolymers*, *Advances in Polymer Science*, Vol. 83 (Springer, Berlin, 1987), pp. 57–192.
[26] R. B. Bird, R. C. Armstrong, and O. Hassager, *Dynamics of Polymeric Liquids*, 2nd ed., Vol. 1 (Wiley, New York, 1987).
[27] M. Dembo and F. Harlow, Biophys. J. **50**, 109 (1986).
[28] N. G. Cogan and R. D. Guy, HFSP J. **4**, 11 (2010).
[29] N. G. Cogan and J. P. Keener, SIAM J. Appl. Math. **65**, 1839 (2005).
[30] M. Dembo, Biophys. J. **55**, 1053 (1989).
[31] H. Brinkman, Appl. Scientific Res. **1**, 27 (1949).
[32] L. Durlofsky and J. Brady, Phys. Fluids **30**, 3329 (1987).
[33] J.-L. Auriault, Transport Porous Media **79**, 215 (2009).
[34] G. I. Bell, Science **200**, 618 (1978).
[35] E. Evans and K. Ritchie, Biophys. J. **72**, 1541 (1997).
[36] K. Keren, P. T. Yam, A. Kinkhabwala, A. Mogilner, and J. A. Theriot, Nat. Cell Biol. **11**, 1219 (2009).
[37] O. T. Fackler and R. Grosse, J. Cell Biol. **181**, 879 (2008).
[38] G. Charras and E. Paluch, Nat. Rev. Mol. Cell Biol. **9**, 730 (2008).